Article

Highly efficient blue InGaN nanoscale light-emitting diodes

https://doi.org/10.1038/s41586-022-04933-5

Received: 27 September 2021

Accepted: 6 June 2022

Published online: 3 August 2022

Check for updates

Mihyang Sheen[1,5]✉, Yunhyuk Ko[1,5], Dong-uk Kim[1,5], Jongil Kim[2], Jin-ho Byun[3], YongSeok Choi[4], Jonghoon Ha[4], Ki Young Yeon[1], Dohyung Kim[1], Jungwoon Jung[1], Jinyoung Choi[1], Ran Kim[1], Jewon Yoo[1], Inpyo Kim[1], Chanwoo Joo[1], Nami Hong[1], Joohee Lee[1], Sang Ho Jeon[1], Sang Ho Oh[2], Jaekwang Lee[3], Nari Ahn[1] & Changhee Lee[1]✉

Indium gallium nitride (InGaN)-based micro-LEDs (μLEDs) are suitable for meeting ever-increasing demands for high-performance displays owing to their high efficiency, brightness and stability[1–5]. However, μLEDs have a large problem in that the external quantum efficiency (EQE) decreases with the size reduction[6–9]. Here we demonstrate a blue InGaN/GaN multiple quantum well (MQW) nanorod-LED (nLED) with high EQE. To overcome the size-dependent EQE reduction problem[8,9], we studied the interaction between the GaN surface and the sidewall passivation layer through various analyses. Minimizing the point defects created during the passivation process is crucial to manufacturing high-performance nLEDs. Notably, the sol–gel method is advantageous for the passivation because SiO_2 nanoparticles are adsorbed on the GaN surface, thereby minimizing its atomic interactions. The fabricated nLEDs showed an EQE of 20.2 ± 0.6%, the highest EQE value ever reported for the LED in the nanoscale. This work opens the way for manufacturing self-emissive nLED displays that can become an enabling technology for next-generation displays.

Light-emitting diodes (LEDs) have been continuously seeing technological advances and are being used in various applications, such as solid-state lightings, displays, optical data communications and photonics[10–13]. In particular, the huge opportunity in the display applications for high brightness and contrast are leading the recent development of micro-LEDs (μLEDs)[3,12,13]. Moreover, rapid growth of the market for augmented reality and extended reality demanding high pixel density per inch (greater than 5,000) and high luminance (more than 10,000 cd m^{-2})[14–17] is also accelerating a shift from a conventional liquid crystal display to the self-emissive μLED displays.

For most display applications, especially high-resolution augmented displays, an LED chip size on the order of micrometres or submicrometres is required[15,16]. However, small-size μLEDs show the size-dependent EQE reduction problem, mainly owing to increased non-radiative recombination loss at the surface as the surface-to-volume ratio increases for smaller chip size[6–9]. Although the surface recombination velocity, a key parameter for surface recombination, of InGaN-based materials (about 3×10^2–10^4 cm s^{-1}) is several orders of magnitude lower than for other III–V semiconductors such as GaAs and InP (ref. [18]), the Shockley–Read–Hall (SRH) recombination at surface defects becomes severe in the micrometre-scale InGaN LEDs[6–10]. In the manufacturing processes of μLEDs, defects, impurities and dangling bonds, which act as non-radiative recombination centres, are generated on the etched surface[7,9,15,16]. It was reported that the EQE of blue InGaN LEDs decreases from about 10% at the lateral dimension of 10 μm down to about 2–3% at the 1-μm size[9]. Therefore, it is essential to develop a technology that minimizes surface defects that occur when manufacturing μm or sub-μm-sized (nanoscale) LEDs and protects the surface with a robust passivation layer.

Development of highly efficient nanoscale LEDs can also make a breakthrough in reducing the manufacturing cost of large-sized display products. The current manufacturing process of μLED displays based on the 'pick-and-place' method has a high manufacturing cost because of slow tact time and low production yield[3]. To overcome this technical challenge, we are developing a new cost-effective method for fabricating nLED displays[19]. The nLEDs were dispersed on the substrate by means of inkjet printing and were horizontally aligned on prepatterned electrodes using dielectrophoretic forces[19–21]. Electric-field-assisted alignment of inkjet-printed nLEDs shortens the process time and lowers the unit cost[19]. This configuration not only increases the light extraction efficiency but also provides control over the luminance by adjusting the number of nLEDs in the pixel. Because the luminance is averaged out over many nLEDs connected in parallel in each pixel, the nLED display is less sensitive to luminance deviation owing to epitaxial defects compared with the μLED display having the pixel with a single μLED. Although the nLED display has a great potential of realizing high-performance displays, the development of highly efficient nLEDs by overcoming the size-dependent EQE reduction problem is a great challenge.

The sidewalls of the InGaN/GaN MQW nanorods contain various structural defects, such as surface dangling bonds, strain-relaxation-induced defects and residual damage from the dry-etch process[6,9,22–24]. It was reported that surface passivation is an effective way to reduce defect states and thereby increase the EQE[22–26]. However, it is inevitable that

[1]Samsung Display, Yongin-si, Republic of Korea. [2]Department of Energy Engineering, KENTECH Institute for Energy Materials and Devices, Korea Institute of Energy Technology (KENTECH), Naju, Republic of Korea. [3]Department of Physics, Pusan National University, Busan, Republic of Korea. [4]Samsung Electronics LED Business Team, Yongin-si, Republic of Korea. [5]These authors contributed equally: Mihyang Sheen, Yunhyuk Ko, Dong-uk Kim. ✉e-mail: mihyang.sheen@samsung.com; chlee7@samsung.com

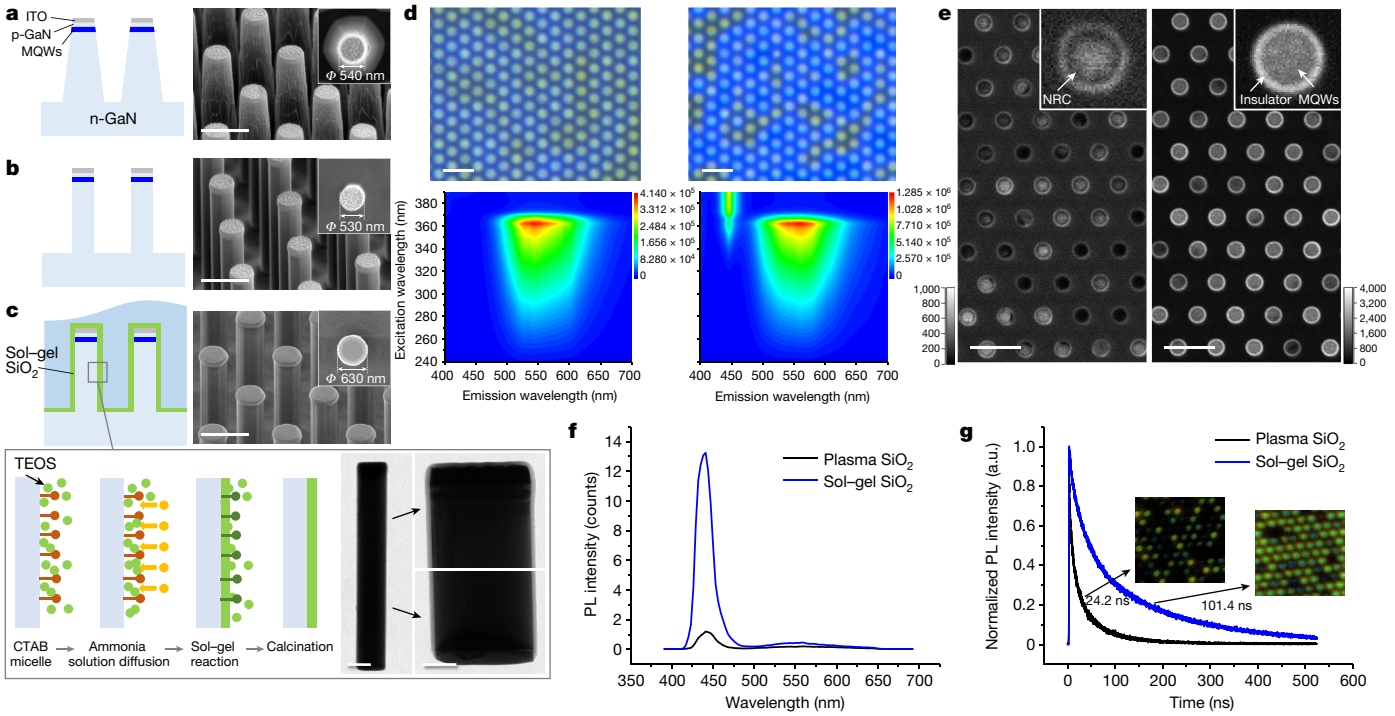

Fig. 1 | Fabrication of nLEDs and their optical properties. a–c, Schematics and corresponding scanning electron microscopy images of nLEDs fabricated by means of conventional top-down processing methods. Dry etching (**a**), wet etching (**b**) and deposition of a SiO_2 surface passivation layer by means of a sol–gel method (**c**). Scale bars, 1 µm. Inset is a schematic of the sol–gel reaction on the GaN LED nanorod. Scale bars, 500 nm (left) and 200 nm (right). **d**, PL image (top; blue and yellow emissions are co-displayed) and fluorescence excitation–emission spectra (bottom) of nanorods with plasma-enhanced ALD SiO_2 passivation (left) and sol–gel SiO_2 passivation (right). Scale bars, 3 µm. **e**, Panchromatic CL images of the submicron LED rod array on wafer with plasma-enhanced ALD SiO_2 (left) and sol–gel SiO_2 (right) (λ = 300–700 nm). Scale bars, 3 µm. **f**, **g**, PL spectra (**f**) and PL decay traces (**g**) of the nanorods averaged over the area indicated in the inset images.

the nLED is exposed to thermal energy, plasma and atomic reactions during the conventional passivation processes of chemical vapour deposition or atomic layer deposition (ALD)[22–25]. As a result, fragile sidewall surfaces are susceptible to structural damages, resulting in the formation of defects.

In this study, we will demonstrate that a low-temperature sol–gel process[27–29] can minimize the formation of defects during the surface passivation process, leading to blue InGaN nanoscale LEDs with a peak EQE of 20.2 ± 0.6%. Considering the trend of the decreasing EQE on size reduction (Extended Data Fig. 1), this is a remarkable achievement and offers the possibility of fabricating highly efficient nLED displays. Using extensive analysis methods such as photoluminescence (PL), electroluminescence (EL), cathodoluminescence (CL) and electron energy-loss spectroscopy (EELS), we identified the defects that cause the performance deterioration in the top-down-processed nLEDs. When the SiO_2 passivation layer is formed with an ALD process, gallium vacancy (V_{Ga}) complex defects are created on the sidewalls of InGaN/GaN nanorods, resulting in the increased SRH recombination and the decreased EQE. This result was cross-validated using X-ray photoelectron spectroscopy (XPS) and deep-level transient spectroscopy (DLTS).

The fabrication process and surface treatment of the nLEDs consisting of an indium tin oxide (ITO)/p-GaN/MQW/n-GaN structure are shown in Fig. 1a–c. The eight pairs of InGaN/GaN MQWs were grown on a 4-inch *c*-plane sapphire substrate. A nanorod pattern with a diameter of about 600 nm was constructed through nanoimprint lithography and then it was dry etched by inductively coupled plasma reactive ion etching. Subsequently, potassium hydroxide (KOH) wet etching was conducted to remove the sidewall damages from the dry-etching process[25,30]. The nanorod shape is transformed from trapezoidal to a vertical cylinder because of the high etching barrier index of the *m*-plane surface[30] and the surfaces of the nanorods become smooth (Fig. 1b).

We applied two insulating layers on the nanorods because a single insulating layer is insufficient to simultaneously achieve the high efficiency, good reliability and processability required for display products. The inner SiO_2 (60 nm thickness) and outer Al_2O_3 (20 nm thickness) layers were used for sidewall passivation and etch stopping during pixel processing, respectively, because of their high transparency, low leakage current and high bandgap energy[31,32]. Optimization of the inner insulating layer, which is directly deposited on the GaN surface, is of utmost importance for achieving highly efficient nLEDs. To minimize the surface damage during the passivation process, we developed a wet-chemical process for synthesizing the SiO_2 passivation layer by means of a sol–gel method, as shown in the inset of Fig. 1c. Performing the sol–gel process at room temperature could minimize the atomic reaction between the GaN surface and the SiO_2 layer and enhance the optical properties of the nanorods by passivating the dangling bonds.

The PL images and the fluorescence excitation–emission spectra (Fig. 1d) and the panchromatic (λ = 300–700 nm) CL images (Fig. 1e) are compared for the nanorods passivated by different methods; conventional plasma-enhanced ALD-deposited SiO_2 (left) and sol–gel-deposited SiO_2 (right). We chose the plasma-enhanced ALD SiO_2 as the reference for comparison with the sol–gel SiO_2 despite its EQE being slightly lower than the thermal ALD SiO_2 because of its superior thin film quality (Extended Data Fig. 2). Compared with the thermal ALD process, the plasma-enhanced ALD produces the SiO_2 layer with lower H_2 outgassing (Extended Data Fig. 2b), which deteriorates the device efficiency during the operation through defect creation, such as Mg–H complexes[33,34]. When the sol–gel process is applied for the SiO_2 passivation, the enhancement of the blue emission over the yellow emission is clearly observed in Fig. 1d. The intensity of the blue emission of the sol–gel SiO_2-passivated nanorods is approximately 13 times higher than that of plasma-enhanced ALD SiO_2-passivated nanorods (Fig. 1f).

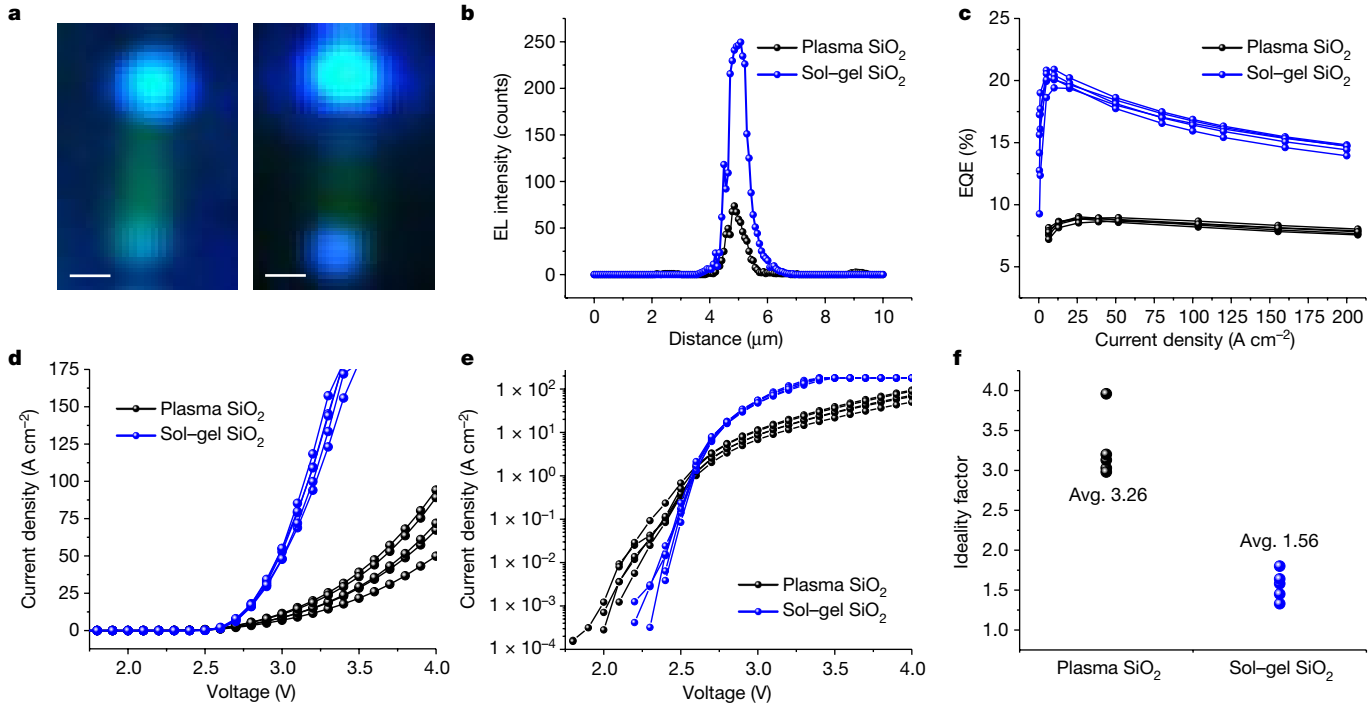

Fig. 2 | Variation in EL and current-density–voltage curves of nLEDs according to the surface passivation method: plasma-enhanced ALD and sol–gel SiO_2 deposition. a, EL and PL composite image of a single nanorod within a pixel based on passivation type: plasma-enhanced ALD SiO_2 (left) and sol–gel SiO_2 (right). Scale bars, 1 μm. **b**, EL intensity profile across the MQWs in the horizontal direction in Fig. 2a, measured with a confocal microscope placed directly above the nanorods. **c**, EQE curves for the nLEDs. Each curve is obtained from 60 pixels, with each pixel comprising six and nine nanorods for plasma-enhanced ALD SiO_2 and sol–gel SiO_2 passivation, respectively. **d**, **e**, The current-density–voltage (*J*–*V*) characteristics of the nLEDs in linear scale (**d**) and log scale (**e**). **f**, Ideality factors obtained from the J–V curves at 2.5 V.

The slight increase of the yellow luminescence (YL) around 550 nm mainly originated from the n-GaN and u-GaN underneath the nanorods (Extended Data Fig. 3) owing to V_{Ga} or substitutional carbon (C_N), and/or its complexes[35–37]. The YL intensity of nanorods dispersed on the wafer is higher than that of the glass specimen for both the plasma-enhanced ALD and sol–gel methods (Extended Data Fig. 3d,h). Furthermore, when we compared the PL spectra of the nanorods itself by normalizing the intensity of the glass specimens (Extended Data Fig. 3j), the YL intensity of the plasma-enhanced ALD SiO_2-passivated nanorods is higher than that of the sol–gel SiO_2-passivated nanorods, indicating that the sol–gel method produces fewer surface defects.

The panchromatic CL images of the individual nanorod LEDs in Fig. 1e clearly visualizes the existence of the non-radiative recombination region depending on the passivation method[36,37]. The outer rim corresponds to the yellow emission from the insulator[38] and the inner circle corresponds to the blue emission of the MQW regions. In the case of plasma-enhanced ALD SiO_2-passivated nanorods (Fig. 1e, left), the outside of the MQWs is darker owing to the non-radiative recombination centre (NRC). Furthermore, the nanorods show marked differences in brightness because of the different positions of the NRC. However, for the sol–gel SiO_2-passivated nanorods (Fig. 1e, right), the overall brightness is uniform and the above-mentioned abnormal light emission is absent. Furthermore, the reduced carrier lifetime of the sol–gel SiO_2-passivated nanorods verifies that the surface defects of GaN are reduced compared with that of the plasma-enhanced ALD-deposited SiO_2 (Fig. 1g).

Figure 2a shows the EL and PL composite images of a single nLED within a pixel according to the passivation method. The pixel is composed of the nLEDs connected in parallel with transparent conductive metals. Because the EL of the horizontally aligned nLED is emitted along the radial and longitudinal directions owing to waveguide reflection, a bright blue and a relatively dark emission are observed at the top and bottom of the nanorods, respectively. The light extraction efficiency (LEE) is calculated for the pixel structure in Extended Data Fig. 4a using a finite-difference time-domain (Ansys Lumerical FDTD) method. The total LEE is approximately 25% and it comprises 71.0% radial emission, 16.8% p-side and 9.9% n-side waveguide emission, and the rest of the optical loss in the transparent electrodes (Extended Data Fig. 4b). The EL intensity profiles obtained from a region horizontally across the top of the nLEDs confirm that the EL intensity of the sol–gel SiO_2-passivated nanorod is higher than that of the plasma-enhanced ALD SiO_2-passivated nanorod (Fig. 2b).

Figure 2c compares the EQE curves for the nLEDs for each surface passivation type. Each curve is obtained from a 60-pixel array (Extended Data Fig. 4c), and each pixel comprises an average of six and nine nLEDs for the plasma-enhanced ALD SiO_2 and sol–gel SiO_2, respectively. The difference in the number of nLEDs per pixel originates from the dispersion in the aligned process. The average values of the peak EQE of the sol–gel and plasma-enhanced ALD SiO_2-deposited nLEDs are 20.2 ± 0.6% and 8.9 ± 0.1%, respectively. Furthermore, the internal quantum efficiency (IQE), calculated by dividing the EQE by the LEE, was 81% and 36% for nLEDs with the sol–gel SiO_2 and plasma-enhanced ALD SiO_2, respectively. The high EQE of the sol–gel SiO_2 nLED is remarkable because it is higher than the best EQE value of the μLED structure even at a larger size[9,23]. The primary reason for such a high EQE is the decreased GaN surface damage in the sol–gel SiO_2 nLED, as confirmed by the longer carrier lifetime in PL and decreased NRC region in CL in Fig. 1.

The nLEDs with the sol–gel SiO_2 show a lower leakage current than that of the plasma-enhanced ALD SiO_2 at below-threshold voltages (Fig. 2d,e) owing to the parallel resistance component attributed to the sidewall damage. This is consistent with the decrease in the ideality factor of nLEDs with the sol–gel SiO_2 compared with that of the plasma-enhanced ALD SiO_2 (Fig. 2f). Generally, the ideality factor of the LED changes greatly depending on its epi-structure[39]. However, we

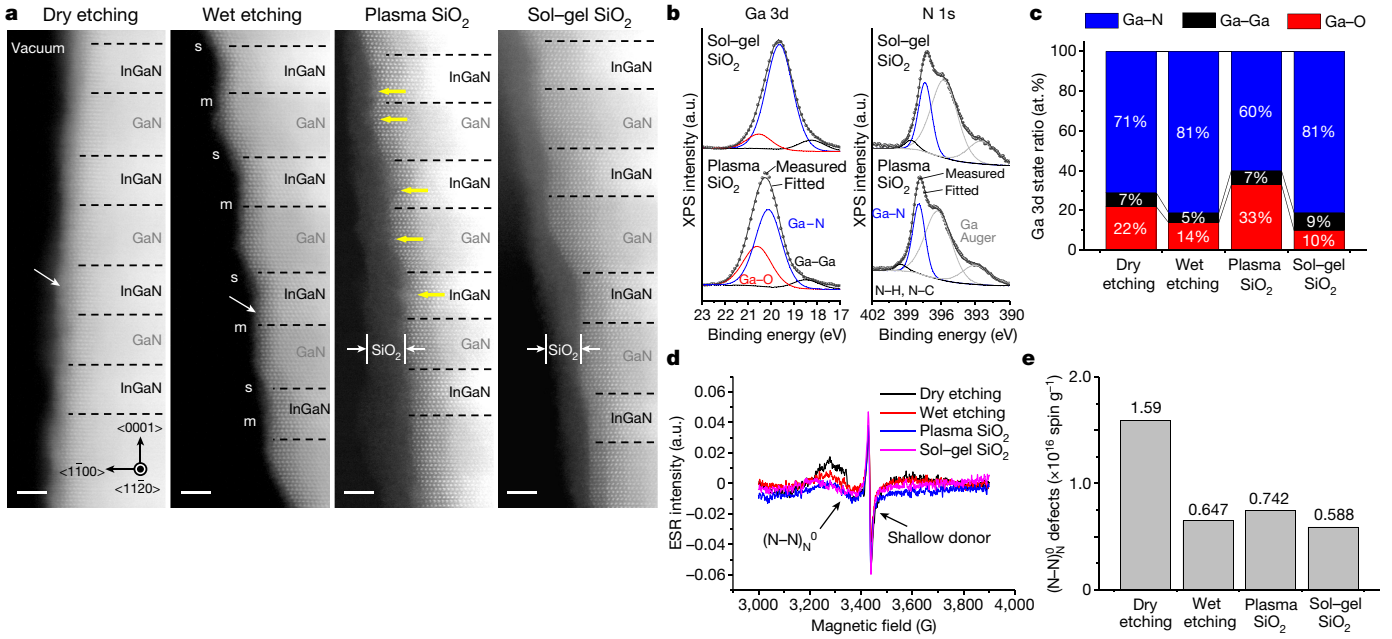

Fig. 3 | Surface analysis of the nLEDs after each fabrication step. **a**, HAADF-STEM images of the sidewall in MQWs according to the fabrication step. The white arrows represent the amorphization of the dry-etched surface. The yellow arrows indicate the plasma damage concentrated on the sidewall of the InGaN quantum wells. Scale bars, 2 nm. **b**, XPS core-level spectra of nLEDs with a 2-nm-thick SiO_2 coating: Ga 3d (left) and N 1s (right). **c**, Ga 3d state ratios obtained from the XPS spectra. **d**, ESR spectra of the nanorods after each fabrication step. **e**, N–N split interstitials of the nanorods based on the ESR spectra.

have proved that the ideality factor can also be changed notably by the passivation method. The decrease in the ideality factor of sol–gel SiO_2 nanorods indicates a decrease in the effective SRH recombination[7,40], thereby increasing the IQE to more than 80%.

The marked change in the electrical and optical properties depending on the sidewall passivation method is closely related to the defects generated during the passivation process. Therefore, understanding the phenomenon occurring at the interface and controlling it are key to manufacturing nLEDs with outstanding performance.

Figure 3 shows the analysis results of the interface between the sidewall of the nanorods and the insulator. The evolution of the morphology and atomic structure of the sidewall in the MQW region after each fabrication step is traced by means of high-angle annular dark-field scanning transmission electron microscopy (HAADF-STEM) imaging (Fig. 3a). After the dry etching of the epi-layer, the nanorod developed a trapezoidal shape owing to the impact-energy difference on the surface. The white arrows indicate the amorphous region at the sidewall, which formed owing to successive ion bombardments. However, after KOH wet etching, the nanorod developed an inverted trapezoidal shape because the etch rate of p-GaN is slower than that of n-GaN (ref. [41]). Furthermore, the semi-polar {10$\bar{1}$1}plane and *m*-plane appear alternately, resulting in a staircase-like sidewall morphology of the InGaN quantum wells. When the SiO_2 layer is deposited through plasma-enhanced ALD, the plasma creates point defects, such as nitrogen vacancies (V_N), nitrogen interstitials (N_i), nitrogen split interstitials $(N–N)_N$, and V_{Ga} and V_{Ga} complexes[42,43], resulting in the amorphization of the surface of the nanorods. This amorphous region is observed on the entire surface of the GaN nanorod. However, it is predominantly observed on the semi-polar facet of the InGaN quantum wells (yellow arrows), probably owing to the high density of dangling bonds. As the thickness of the SiO_2 layer increases from 2 nm to 60 nm (Extended Data Fig. 5e), the penetration depth of the plasma-induced amorphization increases to 4 nm at the InGaN quantum wells. However, when sol–gel SiO_2 is deposited on the nanorods, there is no amorphous region formed at the interface in addition to the deposited SiO_2.

Figure 3b,c and Extended Data Fig. 6b–g show the XPS results. The core-level spectra of Ga 3d could be deconvoluted to the Ga–N, Ga–O and Ga–Ga bonds. The Ga 3d state ratios (Fig. 3c) clearly show that the Ga–O bonds were the highest in the plasma-enhanced ALD SiO_2 nanorods and the lowest in the sol–gel SiO_2 nanorods. Owing to the plasma-induced GaN defects, such as V_N and O_N, the Ga–O bonds increased, whereas the Ga–N bonds decreased. Furthermore, comparing the Si 2p core-level spectrum of sol–gel SiO_2 and plasma-enhanced ALD SiO_2 (Extended Data Fig. 6e), the latter shows oxygen deficiency because of oxygen atoms contributing to the Ga–O bond. Moreover, we obtained electron spin resonance (ESR) spectra to analyse the concentration of the $(N–N)_N$ defects (Fig. 3d,e), which are known as ambipolar defects, that is, with a deep acceptor in n-GaN and a deep donor in p-GaN (ref. [44]). The $(N–N)_N^0$ defects decreased after the wet etching of the nanorods and increased after plasma-enhanced ALD SiO_2 deposition. Because the defect concentrations are calculated by dividing the spins by the total weight of the nanorods and considering that most of the defects are concentrated at the nanorod surface, the actual differences in the defect concentrations of the nanorods after each fabrication step will be greater. Furthermore, the $(N–N)_N^0$ defects in the sol–gel SiO_2-coated nanorods were fewer than those in the wet-etched nanorod, demonstrating the passivation of surface dangling bonds without generating excess defects.

We also carried out DLTS analysis on a bulk LED chip and plasma-enhanced ALD SiO_2-coated nLED-array chip (Extended Data Fig. 7). In the bulk LED chip, the main defects are electron traps owing to V_N and N_i with activation energies of 0.56 and 0.67 eV, respectively[45]. In the nLED-array chip, although the electron trap concentration is similar to that of the bulk LED chip, five types of hole traps (0.14, 0.39, 0.51, 0.56 and 0.93 eV) are observed and the defect concentration is greater than 10^{15} cm^{-3} for the deepest defect level (E_v + 0.93 eV). V_{Ga}-related complexes (complexes of V_{Ga} and oxygen that replace nitrogen sites, that is, $V_{Ga}–O_N$, $V_{Ga}–O_N–2H$) are reportedly responsible for these hole traps[46,47]. According to previous reports[41,48], these V_{Ga} complexes increase the SRH coefficient, thereby increasing the non-radiative recombination rate and markedly decreasing the IQE.

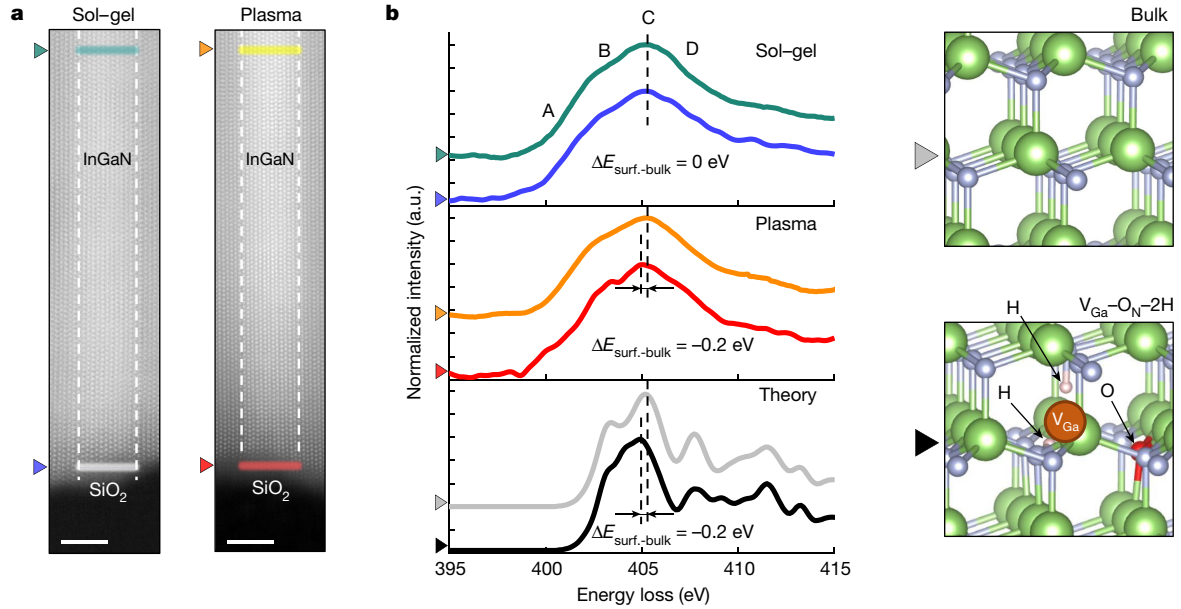

Fig. 4 | Defects in the sidewalls of InGaN quantum wells fabricated using different passivation methods. a, High-resolution STEM images of the InGaN quantum wells. Each coloured layer indicates the region at which the corresponding electron energy loss spectrum was obtained, that is, bulk (green, sol–gel; and yellow, plasma-enhanced ALD) and surface (blue, sol–gel; and red, plasma-enhanced ALD). Scale bars, 2 nm. **b**, N-K-edge spectra of the regions indicated in **a**. Spectral features of the N-K-edge ELNES, which were theoretically verified using DFT calculations, as shown in the bottom panel.

Figure 4 shows a detailed comparison of two representative electron energy loss spectra obtained from the bulk and the surface region of the InGaN quantum wells. For the bulk InGaN, the N-K-edge electron energy-loss near-edge structure (ELNES) can be decomposed into four contributions, denoted by A, B, C and D (ref. [49]). For the InGaN passivated by sol–gel SiO_2, the observed spectral features of N-K ELNES are almost similar for the bulk and surface regions (top panel in Fig 4b). Compared with those of InGaN passivated by the sol–gel method, pronounced changes are observed in the spectral features of the N-K ELNES (red line) of the surface region of InGaN passivated by plasma-enhanced ALD: the appearance of the small peak between the second and third peaks and the chemical shift of the third peak, labelled as C, to a lower energy (red shift).

To theoretically verify the observed spectral features of the N-K ELNES, density functional theory (DFT) calculations were performed by considering the V_{Ga}–O_N–2H complex in a 100-atom-based 3 × 4 × 2 GaN supercell, which corresponds to the most energetically favourable V_{Ga} point defect complexed with O and H (ref. [47]). The main changes caused by the V_{Ga}–O_N–2H complex are that the third peak (C) at approximately 405 eV (bottom-most panel of Fig. 4b) is shifted towards a lower energy by approximately 0.4 eV, and a small shoulder peak appears between B and C at approximately 403 eV, consistent with the experimental results. The red shift and the formation of the shoulder peak suggest that the V_{Ga}–O_N–2H complex locally breaks the wurtzite symmetry by changing the relative distance between the Ga and N atoms and then modifying the hybridization between the Ga and N 2p states, resulting in a chemical shift of the N-K edge and the formation of a shoulder peak. Therefore, we conclude that the V_{Ga}–O_N–2H complex is the dominant defect generated in the sidewalls of the nanorods during the plasma-enhanced ALD SiO_2 passivation, wherein a hydrogen-containing precursor is used.

Although the sol–gel SiO_2 passivation provides superior opto-electrical properties such as high peak EQE of 20.2 ± 0.6% (Fig. 2c), a low leakage current at below-threshold voltages (Fig. 2d,e) and lower ideality factor of 1.56 (Fig. 2f) compared with the plasma-enhanced ALD SiO_2 passivation, it has a few disadvantages, such as the presence of residual reaction by-products. To achieve good reliability, suitable post-treatments are required to complete the reaction and eliminate the reaction residue. We have found that this can be achieved while maintaining the high EQE by baking the sol–gel SiO_2 film (Extended Data Fig. 8). With these preliminary results, research on further improvement through process optimization is now under way.

In conclusion, we developed blue InGaN nLEDs with high peak EQE of 20.2 ± 0.6% by means of sol–gel SiO_2 passivation. The nanorods were aligned on prepatterned electrodes using the dielectrophoretic force and connected in parallel through transparent electrodes in each pixel. We demonstrated that passivation by means of conventional plasma-enhanced ALD induces amorphization at the InGaN quantum well surfaces and creates point defects on the sidewalls of GaN nanorods, which increases the SRH recombination and generates an NRC region at the InGaN sidewall of the nanorods. The sol–gel process provides effective passivation for the GaN surfaces because the SiO_2 nanoparticles are adsorbed on the GaN surface after the sol–gel reaction. Thus, the atomic interaction with the GaN surface is minimized and only dangling bonds of the surfaces are passivated, resulting in a low leakage current, decreased NRC regions and high EQE. We believe that our findings will accelerate the implementation of nLEDs in next-generation displays.

Online content

Any methods, additional references, Nature Research reporting summaries, source data, extended data, supplementary information, acknowledgements, peer review information; details of author contributions and competing interests; and statements of data and code availability are available at https://doi.org/10.1038/s41586-022-04933-5.

1. Lin, J. Y. & Jiang, H. X. Development of microLED. *Appl. Phys. Lett.* **116**, 100502 (2020).
2. Wierer Jr., J. J. & Tansu, N. III-nitride micro-LEDs for efficient emissive displays. *Laser Photonics Rev.* **13**, 1900141 (2019).
3. Virey, E. H. & Baron, N. 45-1: Status and prospects of microLED displays. *SID Symp. Dig. Tech. Pap.* **49**, 593–596 (2018).
4. Templier, F. GaN-based emissive microdisplays: a very promising technology for compact, ultra-high brightness display systems. *J. Soc. Inf. Display* **24**, 669–675 (2016).
5. Jiang, H. X. & Lin, J. Y. Nitride micro-LEDs and beyond—a decade progress review. *Opt. Express* **21**, A475–A484 (2013).
6. Olivier, F. et al. Influence of size-reduction on the performances of GaN-based micro-LEDs for display application. *J. Lumin.* **191**, 112–116 (2017).

7. Hwang, D. et al. Sustained high external quantum efficiency in ultrasmall blue III–nitride micro-LEDs. *Appl. Phys. Express* **10**, 032101 (2017).
8. Konoplev, S. S., Bulashevich, K. A. & Karpov, S. Y. From large-size to micro-LEDs: scaling trends revealed by modeling. *Phys. Status Solidi A* **215**, 1700508 (2018).
9. Smith, J. M. et al. Comparison of size-dependent characteristics of blue and green InGaN microLEDs down to 1 μm diameter. *Appl. Phys. Lett.* **116**, 071102 (2020).
10. Schubert, E. F. *Light-Emitting Diodes* (Cambridge Univ. Press, 2006).
11. Ren, A. et al. Emerging light-emitting diodes for next-generation data communications. *Nat. Electron.* **4**, 559–572 (2021).
12. Biwa, G. et al. Technologies for the Crystal LED display system. *J. Soc. Inf. Display* **29**, 435–445 (2021).
13. Huang, Y. et al. Mini-LED, micro-LED and OLED displays: present status and future perspectives. *Light Sci. Appl.* **9**, 105 (2020).
14. Kawanishi, H. et al. High-resolution and high-brightness full-colour "Silicon Display" for augmented and mixed reality. *J. Soc. Inf. Display* **29**, 57–67 (2021).
15. Xiong, J. et al. Augmented reality and virtual reality displays: emerging technologies and future perspectives. *Light Sci. Appl.* **10**, 216 (2021).
16. Liu, Z. et al. Micro-light-emitting diodes with quantum dots in display technology. *Light Sci. Appl.* **9**, 83 (2020).
17. Zhang, L. et al. 31.1: Invited Paper: Monochromatic active matrix micro-LED micro-displays with >5,000 dpi pixel density fabricated using monolithic hybrid integration process. *SID Symp. Dig. Tech. Pap.* **49**, 333–336 (2018).
18. Bulashevich, K. A. & Karpov, S. Y. Impact of surface recombination on efficiency of III-nitride light-emitting diodes. *Phys. Status Solidi RRL* **10**, 480–484 (2016).
19. Sung, Y. G. Micro-led element for horizontally-aligned assembly, method for manufacturing same, and horizontally-aligned assembly comprising same. US patent US20170317228A1 (2017).
20. Park, H., Kim, B.-J. & Kim, J. Electroluminescence from InGaN/GaN multiquantum-wells nanorods light-emitting diodes positioned by non-uniform electric fields. *Opt. Express* **20**, 25249–25254 (2012).
21. Park, H. et al. Horizontally assembled green InGaN nanorod LEDs: scalable polarized surface emitting LEDs using electric-field assisted assembly. *Sci. Rep.* **6**, 28312 (2016).
22. Yang, C. et al. Enhancement in light extraction efficiency of GaN-based light-emitting diodes using double dielectric surface passivation. *Opt. Photonics J.* **2**, 185–192 (2012).
23. Bai, J. et al. Ultrasmall, ultracompact and ultrahigh efficient InGaN micro light emitting diodes (μLEDs) with narrow spectral line width. *ACS Nano* **14**, 6906–6911 (2020).
24. Wong, M. S. et al. High efficiency of III-nitride micro-light-emitting diodes by sidewall passivation using atomic layer deposition. *Opt. Express* **26**, 21324–21331 (2018).
25. Wong, M. S. et al. Size-independent peak efficiency of III-nitride micro-light-emitting-diodes using chemical treatment and sidewall passivation. *Appl. Phys. Express* **12**, 097004 (2019).
26. Ley, R. T. et al. Revealing the importance of light extraction efficiency in InGaN/GaN microLEDs via chemical treatment and dielectric passivation. *Appl. Phys. Lett.* **116**, 251104 (2020).
27. Dubey, R., Rajesh, Y. & More, M. Synthesis and characterization of SiO_2 nanoparticles via sol-gel method for industrial applications. *Mater. Today Proc.* **2**, 3575–3579 (2015).
28. Azlina, H., Hasnidawani, J., Norita, H. & Surip, S. Synthesis of SiO_2 nanostructures using sol-gel method. *Acta Phys. Pol. A* **129**, 842–844 (2016).
29. Zhang, W. et al. Preparation of SiO_2 anti-reflection coatings by sol-gel method. *Energy Procedia* **130**, 72–76 (2017).
30. Lai, Y.-Y. et al. The study of wet etching on GaN surface by potassium hydroxide solution. *Res. Chem. Intermed.* **43**, 3563–3572 (2017).
31. Peñalba, M., Juaristi, J., Zarate, E., Arnau, A. & Bauer, P. Electronic stopping power of Al_2O_3 and SiO_2 for H, He, and N. *Phys. Rev. A* **64**, 012902 (2001).
32. Wilk, G. D., Wallace, R. M. & Anthony, J. High-κ gate dielectrics: current status and materials properties considerations. *J. Appl. Phys.* **89**, 5243–5275 (2001).
33. Lee, D., Mitchell, B., Fujiwara, Y. & Dierolf, V. Thermodynamics and kinetics of three Mg–H–V_N complexes in Mg:GaN from combined first-principles calculation and experiment. *Phys. Rev. Lett.* **112**, 205501 (2014).
34. Miceli, G. & Pasquarello, A. Self-compensation due to point defects in Mg-doped GaN. *Phys. Rev. B* **93**, 165207 (2016).
35. Lyons, J. L., Alkauskas, A., Janotti, A. & Van de Walle, C. G. First-principles theory of acceptors in nitride semiconductors. *Phys. Status Solidi B* **252**, 900–908 (2015).
36. Reshchikov, M. A. & Morkoç, H. Luminescence properties of defects in GaN. *J. Appl. Phys.* **97**, 061301 (2005).
37. Liu, B. et al. Origin of yellow-band emission in epitaxially grown GaN nanowire arrays. *ACS Appl. Mater. Interfaces* **6**, 14159–14166 (2014).
38. Koyama, H. Cathodoluminescence study of SiO_2. *J. Appl. Phys.* **51**, 2228–2235 (1980).
39. Zhu, D. et al. The origin of the high diode-ideality factors in GaInN/GaN multiple quantum well light-emitting diodes. *Appl. Phys. Lett.* **94**, 081113 (2009).
40. Tian, P. et al. Size-dependent efficiency and efficiency droop of blue InGaN micro-light emitting diodes. *Appl. Phys. Lett.* **101**, 231110 (2012).
41. Zhuang, D. & Edgar, J. H. Wet etching of GaN, AlN, and SiC: a review. *Mater. Sci. Eng. R Rep.* **48**, 1–46 (2005).
42. Foster, G. M. et al. Recovery from plasma etching-induced nitrogen vacancies in p-type gallium nitride using UV/O_3 treatments. *Appl. Phys. Lett.* **117**, 082103 (2020).
43. Kato, M. et al. Characterization of plasma etching damage on p-type GaN using Schottky diodes. *J. Appl. Phys.* **103**, 093701 (2008).
44. Von Bardeleben, H. J. et al. Identification of the nitrogen split interstitial $(N–N)_N$ in GaN. *Phys. Rev. Lett.* **109**, 206402 (2012).
45. Reshchikov, M. A. et al. Evaluation of the concentration of point defects in GaN. *Sci. Rep.* **7**, 9297 (2017).
46. Wickramaratne, D. et al. Defect identification based on first-principles calculations for deep level transient spectroscopy. *Appl. Phys. Lett.* **113**, 192106 (2018).
47. Dreyer, C. E. et al. Gallium vacancy complexes as a cause of Shockley-Read-Hall recombination in III-nitride light emitters. *Appl. Phys. Lett.* **108**, 141101 (2016).
48. Lyons, J. L. & Van de Walle, C. G. Computationally predicted energies and properties of defects in GaN. *NPJ Comput. Mater.* **3**, 12 (2017).
49. Mizoguchi, T. et al. First-principles calculations of ELNES and XANES of selected wide-gap materials: dependence on crystal structure and orientation. *Phys. Rev. B* **70**, 045103 (2004).

Methods

Fabrication of top-down-processed nLEDs

We used commercially grown 4-inch epitaxial wafers, produced by the Samsung Electronics LED Business Team. They had eight pairs of InGaN/GaN MQW LED structures on *c*-plane sapphire substrates. An ITO layer (110 nm thick) was deposited on top of the p-type GaN to obtain a p-type transparent conducting electrode. Nanoimprint lithography was performed to fabricate a rod-like pattern using a SiO_2-based hard mask on the ITO layer, and this pattern was dry etched using inductively coupled plasma reactive ion etching. Subsequently, KOH wet etching was conducted to remove the surfaces of the mesa that were damaged during the dry-etching process. Then the nanorod surface was passivated by two insulating layers with the 60-nm-thick SiO_2 inner layer for sidewall passivation and the 20-nm-thick Al_2O_3 outer layer for etch stopping during pixel processing. The average diameter and length of the fabricated nanorods were about 580 nm and 4 μm, respectively. The nanorods were separated from the wafer using a diamond cutter. The separated nanorods were then dispersed in solvents for depositing in the pixel area using an inkjet printing method. As shown in the schematic diagram in Extended Data Fig. 4a, the nanorods were placed between two bottom electrodes, which were used to align the nanorods horizontally by applying the dielectrophoretic force[19–21]. The top transparent electrodes were connected with the nanorods for electrical biasing.

Synthesis of SiO_2 passivation layer by means of the sol–gel method

Tetraethyl orthosilicate (TEOS, Sigma-Aldrich, 98%) was used as a precursor for the synthesis of a SiO_2 passivation layer on the surface of nanorods. A schematic of the entire sol–gel process is shown in Fig. 1c. First, 210 ml of ethanol (EtOH, Sigma-Aldrich, anhydrous) and 290 ml of deionized water were mixed in a three-necked flask. The entire 4-inch wafer with nanorods was dipped in this solution. Then, 0.8 g of cetyltrimethylammonium bromide (CTAB, Sigma-Aldrich, ≥98%) was dissolved in the solution at room temperature to form micelles. After stirring the above mixture at 500 rpm for 5 min, 2.5 ml of an aqueous ammonia solution (Sigma-Aldrich, 28–30%) and 1.25 ml of TEOS were sequentially added dropwise into the reactants. The resulting mixture was then continuously stirred at 25 °C at 500 rpm for 2 h and the wafer was washed with deionized water and EtOH. The thickness of the SiO_2 layer increased linearly with an increase in the reaction time for 60 min and saturated at 23 nm owing to the limited quantity of sol particles (Extended Data Fig. 9g). The transmission electron microscopy image in the inset of Fig. 1c shows a well-defined and uniform SiO_2 layer on the nanorods from the top to bottom. By repeating the sol–gel reaction, the thickness of the SiO_2 layer increases. The PL intensity increased on doubling the thickness of the SiO_2 layer (Extended Data Fig. 9h) and then saturated. It is attributed to the reduction of defects and effective passivation of the dangling bonds (Extended Data Fig. 5c). To evaluate the passivation uniformity, we recorded the PL spectra from three different positions on the 4-inch wafer. We found that the variation in the PL intensity with respect to the position is minor.

PL analysis of nanorods and nLEDs in the pixel structure

Two-dimensional steady-state PL spectra were obtained using a FluoroMax-4 spectrofluorometer (Horiba) with a 150-W ozone-free xenon arc lamp as the excitation source. Steady-state PL/EL images and a two-photon spectrum of GaN nanorods were obtained using a modified confocal microscope (Leica TCS SP8). The excitation sources were an enhanced mercury arc lamp with a bandpass filter (λ = 340–380 nm) and a Ti:sapphire laser (Chameleon Vision) producing 140-fs pulses at a repetition rate of 80 MHz for the steady-state PL images and two-photon spectrum, respectively. An excitation wavelength of 740 nm was used for the two-photon excitation of InGaN MQWs. The lamp and laser were focused through a dry objective (NA 0.8). For the PL images in Fig. 1 and Extended Data Fig. 3, we applied a long-pass filter (λ > 425 nm) to acquire the blue and yellow overlapped image. To avoid the PL saturation for the sol–gel SiO_2 nanorods, in Fig. 1d, we applied an attenuator to reduce the light intensity by a quarter. The PL decay traces and fluorescence lifetime images were obtained using another modified confocal microscope (Leica TCS SP8) with PicoHarp 300 (PicoQuant) by using the time-correlated single-photon counting technique. They were obtained by the one-photon excitation of a 405-nm diode laser at a repetition rate of 625 kHz. The objective lens was the same as that used in the steady-state PL measurements. All PL and EL measurements were performed at room temperature between 20 and 25 °C in a dark room. The PL and EL spectra for the plasma-enhanced ALD SiO_2 passivation and sol–gel SiO_2 passivation were compared in Extended Data Fig. 10. The red-shifted EL spectrum compared with the PL spectrum can be attributed to the influence of surface defects and different quantum confinement process between photoexcitation and electrical excitation. The EL spectrum broadening in the plasma SiO_2-passivated device can be explained as the result of the increased dispersion owing to surface defects. The plasma SiO_2 passivation generates more surface defects compared with the sol–gel SiO_2 passivation or KOH wet etching (Fig. 3 and Extended Data Fig. 11).

Quantification of defect concentrations using ESR

ESR measurements were performed using an X-band Bruker ELEXSYS-II E500 spectrometer. A helium gas flow cryostat was used at an operating temperature of 6 K. The GaN nanorod powder samples were placed in a quartz sample tube with a diameter of 4 mm and held in a microwave cavity. The experimental ESR settings were as follows: microwave power 0.002 mW; sweep width 1,000 G; modulation frequency 100 kHz; modulation amplitude 5 G; sweep time 200 s; number of points 2,048; number of scans 8. The spin density was calculated using the SpinCount/SpinFit software.

Surface-state analysis using XPS

The XPS data were obtained using an ESCALAB 250Xi electron spectrometer (Thermo Fisher Scientific) with a monochromatic Al-Kα X-ray (1,486.7 eV) source and a spot size of 400 μm. To obtain the Ga 3d and N 1s core-level spectra of the nanorod sidewall, the SiO_2 insulating layer was intentionally deposited with a thickness of only 2 nm using plasma-enhanced ALD and sol–gel synthesis. Then, the nanorods were separated from the wafer and dispersed on the Si substrate. Atomic concentrations were determined from the survey spectra (0–1,350 eV, 10 eV detector pass energy, 1 eV step size, 50 ms dwell time, two scans). Furthermore, high-resolution spectra were acquired (20 eV detector pass energy, 0.1 eV step size, 50 ms dwell time, ten scans) and the Thermo Fisher Scientific Avantage software was used for peak fitting; the Smart background option was used. The spectrometer was calibrated using the C 1s peak as a reference point (284.8 eV), which is in excellent agreement with the average values provided by the National Institute of Standards and Technology (NIST).

Trap-density analysis using DLTS

All the DLTS measurements in this study were conducted using a DLS-1100 (SEMILAB) system in the temperature range 80–600 K. The chips in which approximately 10,000 nanorods were p–n aligned in an area of 500 μm^2 were loaded in the DLTS chamber at a vacuum of 1×10^{-2} torr. The measurement conditions were a temperature scan of 100 mK s^{-1} and a pulse voltage of 2 V to facilitate the formation of the depletion region in the nanorod device.

Measurement of electrical properties and EQE of nLEDs and LEE simulation

The current density–voltage (J–V) curves for a single pixel in test element group (TEG) cells were recorded using a Keithley 2400 source

measurement unit (Keithley Instruments). The ideality factor of the diode characteristics was calculated from the intermediate range of the J–V curves as shown in Extended Data Fig. 12. The EQE was measured for the TEG cell using a CAS 140CT Array Spectroradiometer (Konica Minolta) with an integrating sphere (ISP 40-101), which was calibrated with a standard light source (Extended Data Fig. 4c,d). The optical field distribution in Extended Data Fig. 4b was calculated for the pixel structure in Extended Data Fig. 4a with the simulation area of $30 \times 30 \times 5\ \mu m^3$ using an FDTD method (Ansys Lumerical). Isotropic dipoles from MQWs were used as a light source and the total amount of light emitted out of the pixel is defined as the LEE. The IQE was obtained by dividing the EQE by the LEE.

Observation of surface atomic structure using transmission electron microscopy

We used an aberration-corrected STEM system (Themis Z G3, Thermo Fisher Scientific) with an accelerated electron beam of 300 kV to observe the atomic structure of the sidewall region. The nanorods were directly dispersed on lacey carbon grids to prevent damage to Ga ions during focused ion beam (FIB) milling of the specimen. Furthermore, the insulating layer was intentionally deposited with a thickness of only 2 nm for electron transparency. To observe the interface between the nanorods and the SiO_2 layer, we performed STEM-EELS (JEM-ARM200F, JEOL) measurement on an FIB specimen with 60-nm-thick SiO_2-deposited nanorods. Further, we cleaned the specimen using an Ar-ion beam to remove the areas that sustained Ga-ion damage during FIB.

Electron energy-loss spectroscopic analysis

EELS calculations were performed on the basis of the DFT implemented in VASP[50]. The projector augmented-wave method was used to mimic the ionic functional[51], whereas the Perdew–Burke–Ernzerhof approximation was used for the electron exchange-correlation functional[52]. Plane waves were included up to an energy cut-off of 400 eV. We used a $9.0 \times 11 \times 11$-Å supercell to consider defect complexes. The Brillouin zone for the supercell calculation was sampled using a $2 \times 2 \times 2$ k-point grid. Ionic and electronic relaxations were performed by applying a convergence criterion of 5×10^{-2} eV Å^{-1} per ion and 10^{-5} eV per electronic step. The supercell core–hole method was used to obtain the electron energy loss spectra of GaN (ref. [53]). The core electron of the oxygen atom was removed from the core and added to the valence/conduction bands, resembling the final state of the excitation process (also referred to as final-state approximation). We used a constant Lorentzian broadening of 0.5 eV to replicate the experimental broadening.

Data availability

All data generated or analysed during this study are included in the paper.

Code availability

We used the commercially available software of Ansys Lumerical for the FDTD simulation and VASP for the DFT calculations. The simulation settings are presented in Methods. The atomic structure data for the defects are available at Zenodo, https://doi.org/10.5281/zenodo.6544988.

50. Kresse, G. & Furthmüller, J. Efficient iterative schemes for ab initio total-energy calculations using a plane-wave basis set. *Phys. Rev. B* **54**, 11169 (1996).
51. Blöchl, P. E. Projector augmented-wave method. *Phys. Rev. B* **50**, 17953 (1994).
52. Perdew, J. P., Burke, K. & Ernzerhof, M. Generalized gradient approximation made simple. *Phys. Rev. Lett.* **77**, 3865 (1996).
53. Karsai, F. et al. Effects of electron-phonon coupling on absorption spectrum: *K* edge of hexagonal boron nitride. *Phys. Rev. B* **98**, 235205 (2018).

Acknowledgements We thank J. Kwag and D. Kim for encouragement and full support; Y. Choi and S. Yoon for support and technical advice on nLED fabrication; S.-C. Jo for his valuable advice; H. Cho for his help in nLED fabrication and characterization; H. Cha and S. Kim for their assistance with testing nLEDs; Y. Han and Y. Shim for the LEE simulation; M. Kim at Seoul National University for the deeply insightful discussion.

Author contributions Y.C. and J.H. prepared the epi-wafer and fabricated the nanorods. D.-u.K. and J.Y. fabricated the nLEDs and the pixels using the nanorods. Y.K., I.K., C.J. and N.H. synthesized the sol–gel SiO_2 layer on the nanorods. J.K. and J.-h.B. analysed and interpreted the STEM-EELS data. K.Y.Y., D.K., J.J., J.C. and R.K. carried out the PL, DLTS, ESR and XPS analyses. Joohee Lee and S.H.J. calculated the defect levels of GaN. S.H.O. and Jaekwang Lee contributed to the interpretation of the experimental results and calculated the data. N.A. and C.L. supervised the research and coordinated the work. M.S. contributed to the experiments and analyses. M.S. and C.L. wrote the manuscript, with input from all other authors.

Competing interests The authors declare no competing interests.

Additional information
Correspondence and requests for materials should be addressed to Mihyang Sheen or Changhee Lee.

Peer review information *Nature* thanks Steven DenBaars, Zhaojun Liu and Shin-Tson Wu for their contribution to the peer review of this work.

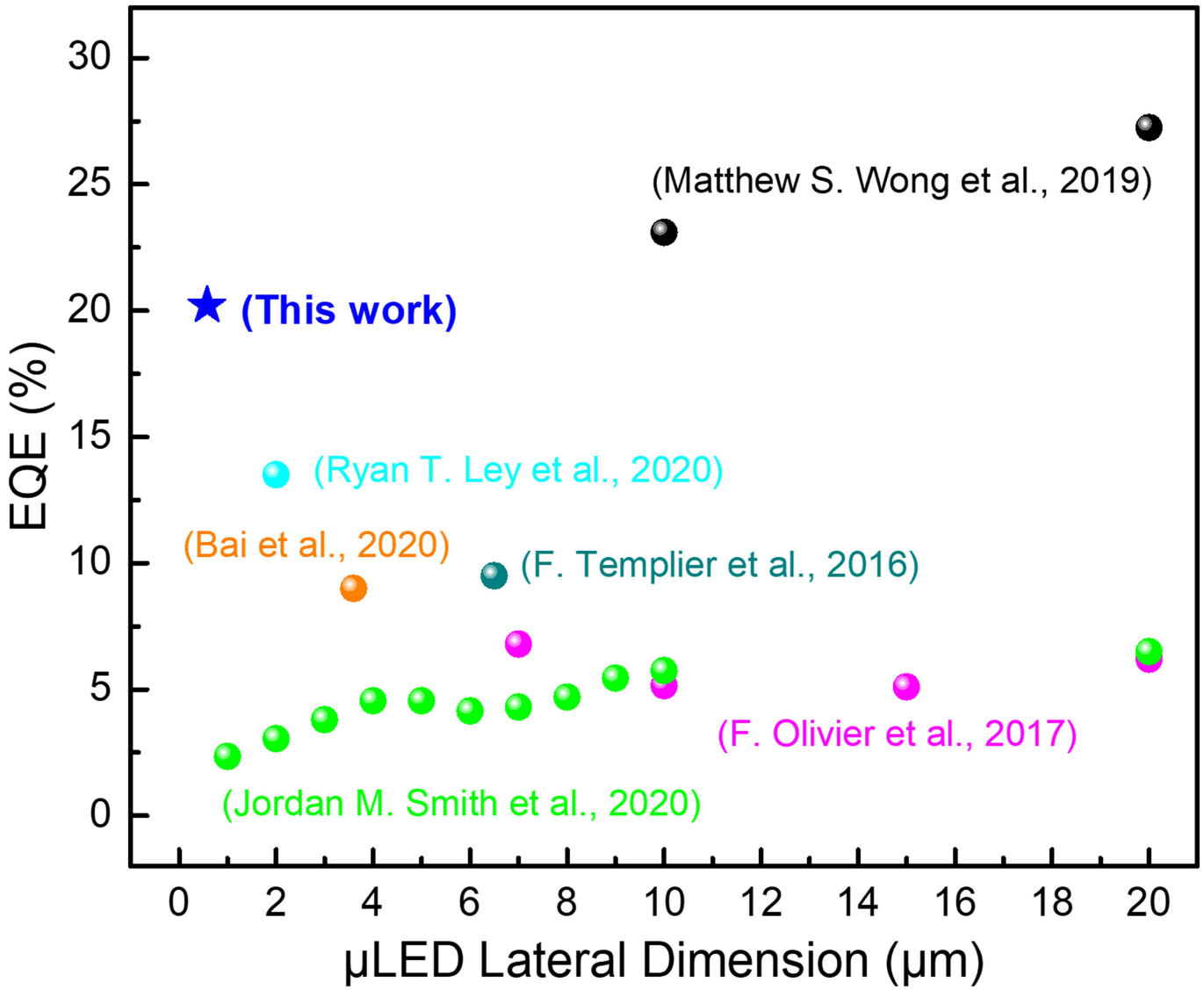

Extended Data Fig. 1 | Size-dependent EQE of μLEDs. The EQE values are presented according to recent results in the literature.

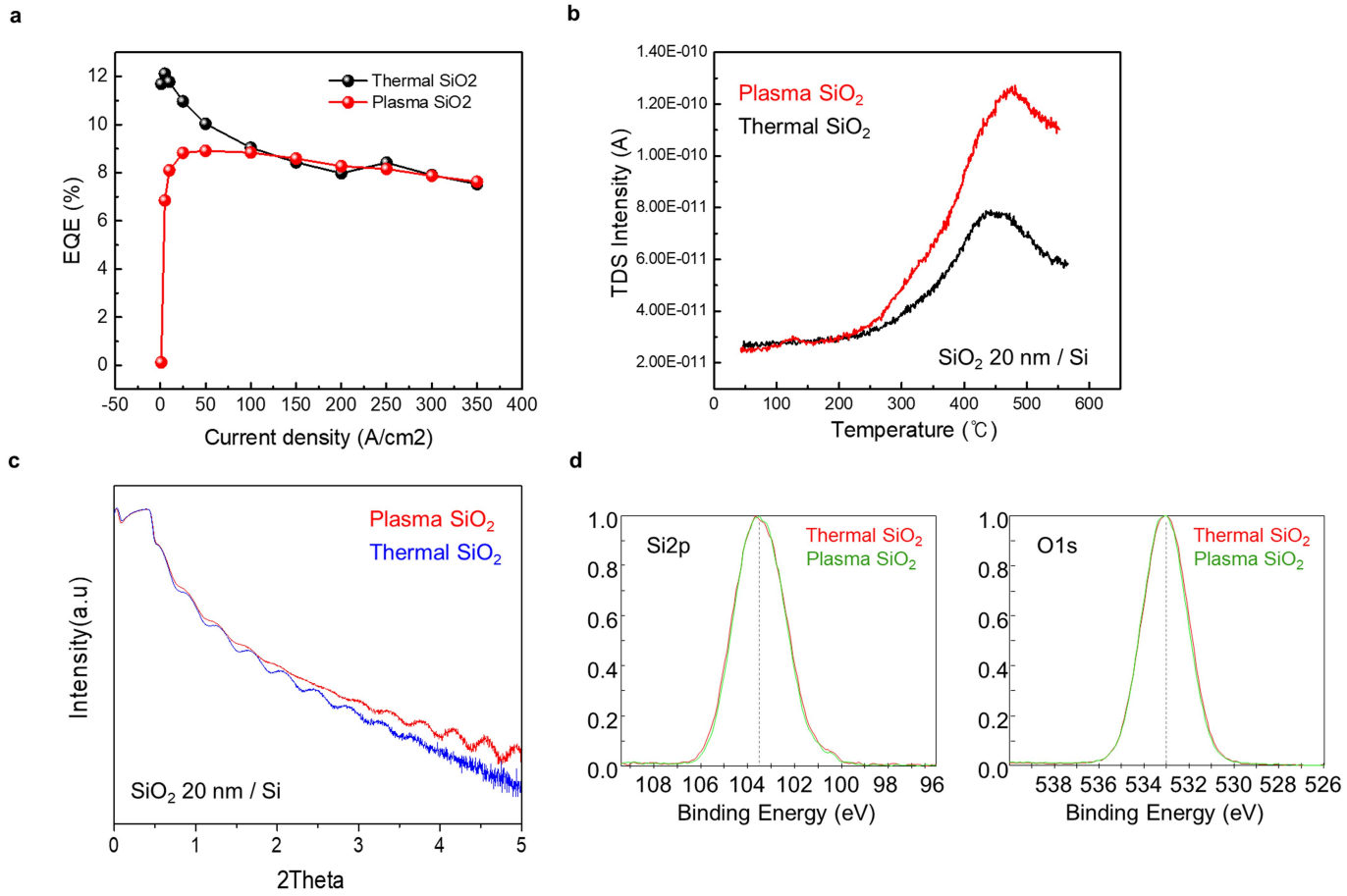

Extended Data Fig. 2 | Comparison between thermal ALD SiO_2 and plasma-enhanced ALD SiO_2 passivation. a, EQE curves for the nLEDs with the 60-nm-thick SiO_2 passivation layer deposited with thermal ALD and plasma-enhanced ALD processes. **b**, Thermal desorption spectroscopy (TDS) for measuring H_2 outgassing. **c**, X-ray reflectivity measurement for thin-film density. **d**, XPS core-level spectra for Si 2p and O 1s obtained from a 20-nm-thick SiO_2 layer deposited on a Si substrate with thermal ALD and plasma-assisted ALD processes.

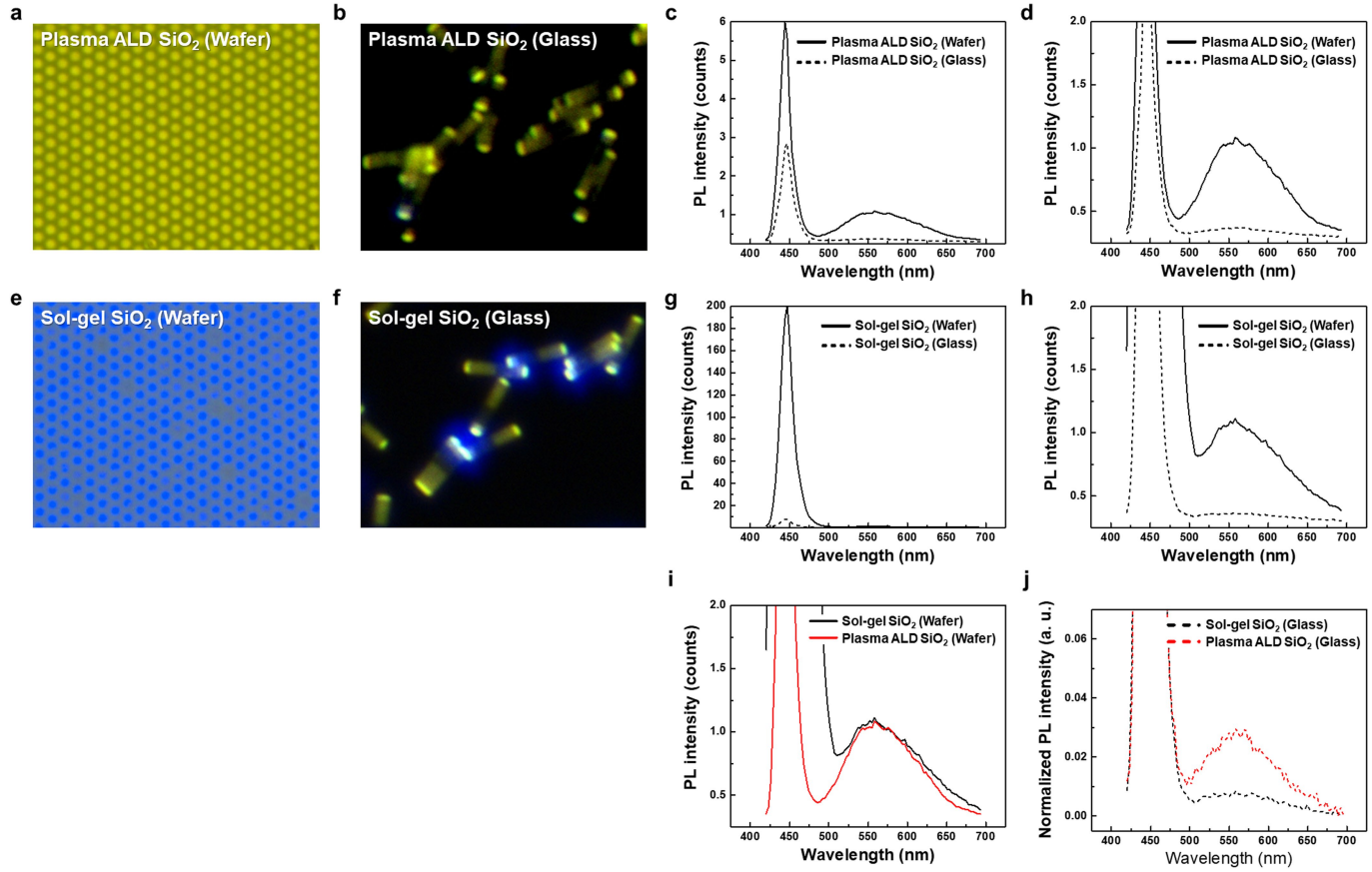

Extended Data Fig. 3 | Influence of the GaN substrate on yellow luminescence in the PL spectra of nanorods. a, **b**, PL images of the plasma-enhanced ALD SiO_2 (60 nm thickness) coated nanorods dispersed on wafer (**a**) and glass (**b**). The PL spectra from the wafer and glass specimens are compared in **c**. The YL region of the PL spectra are enlarged in **d**. The sol–gel SiO_2 (25 nm thickness) coated nanorods are presented in **e**–**h** in the same manner. The YL is compared in **i** for the wafer specimen and in **j** for the glass specimen.

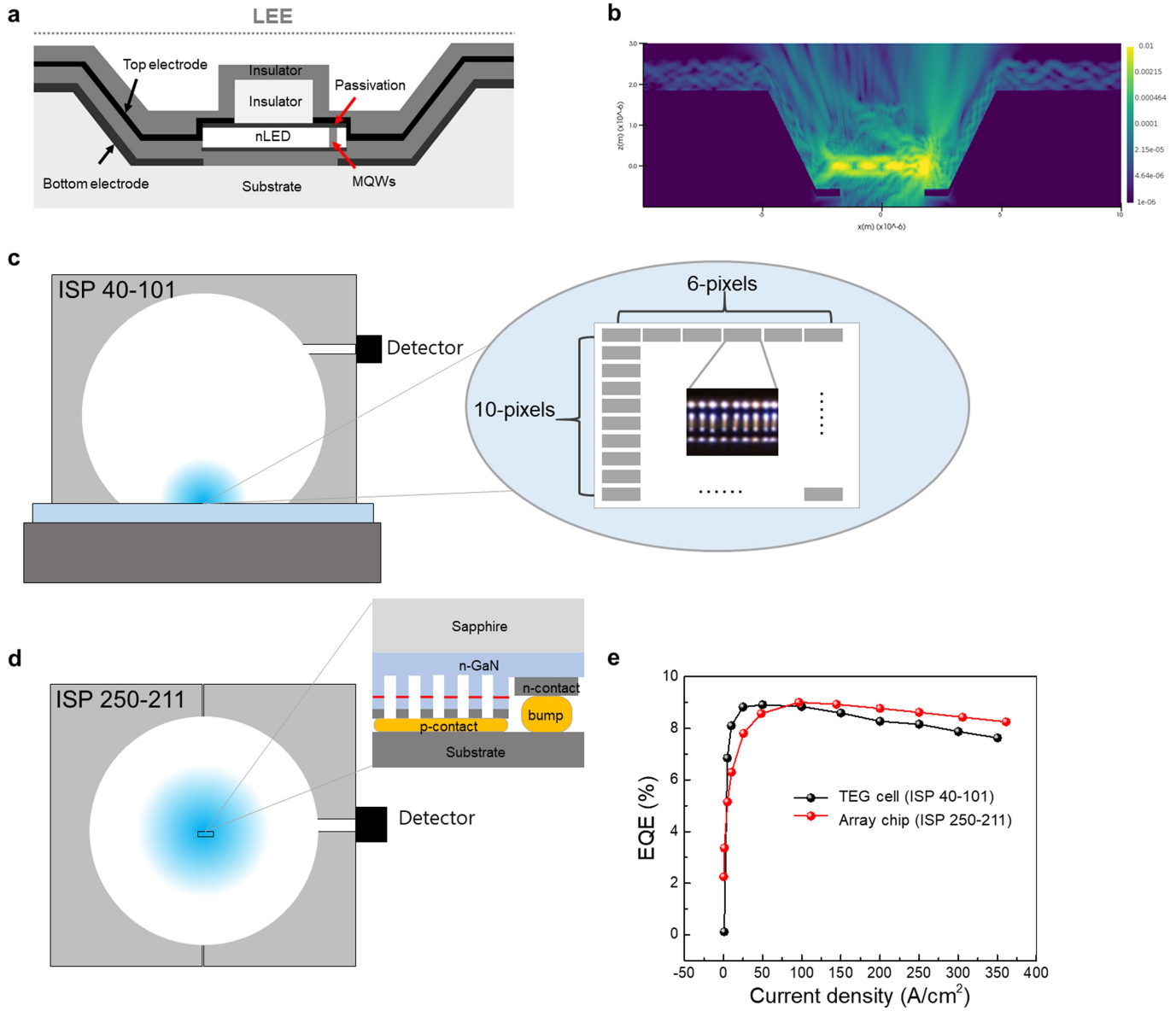

Extended Data Fig. 4 | LEE simulation and EQE measurement set-up for nLED devices. a, Schematic diagram of the nLED pixel structure. **b**, Cross-sectional optical field distribution of the nLED device. **c**, Schematic diagram of the EQE measurement with an integrating sphere (ISP 40-101) and calibrated spectroradiometer system for the nLED TEG cell. Each TEG cell is composed of 60 pixels and each pixel is composed of 6–9 nanorods connected in parallel. **d**, Schematic diagram of the EQE measurement with a full integrating sphere (ISP 250-211) and calibrated spectroradiometer system for the nLED-array chip. **e**, EQE curves measured in the configurations of **c** and **d** are compared for the 60-nm-thick SiO_2 passivation layer deposited with the plasma-enhanced ALD process.

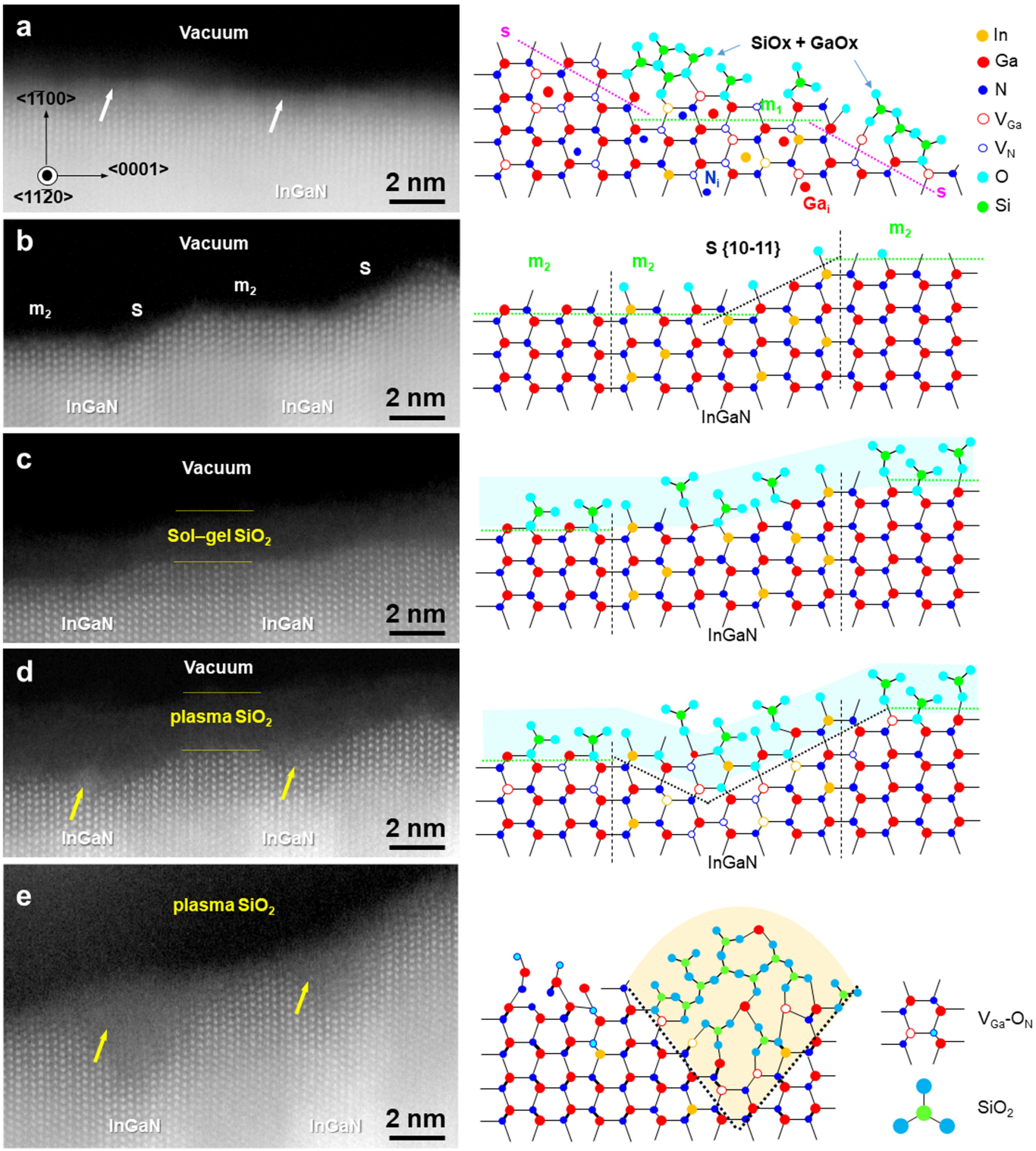

Extended Data Fig. 5 | Atomic structure between the GaN surface and SiO_2 insulator. a–**e**, STEM-HAADF images of the MQWs in the sidewall region according to the fabrication steps, that is, dry etch (**a**), wet etch (**b**), sol–gel SiO_2 deposition (**c**) and plasma-enhanced ALD SiO_2 deposition of thicknesses of 2 nm (**d**) and 60 nm (**e**). The increase in the plasma-induced amorphization at the quantum well sidewall with increasing thickness of the SiO_2 layer from 2 nm (**d**) to 60 nm (**e**) is evident.

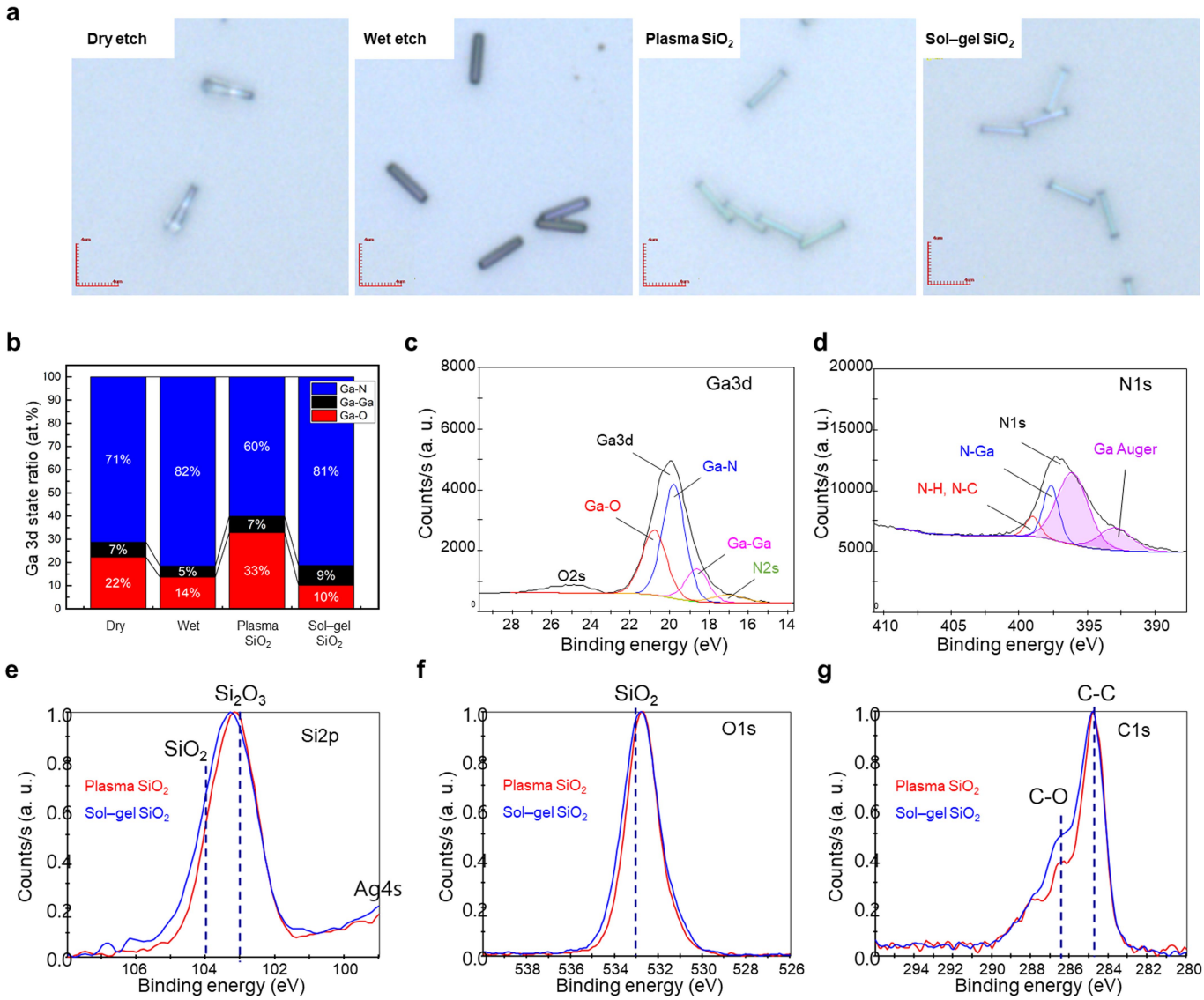

Extended Data Fig. 6 | Surface defects of nLEDs according to their fabrication steps. a, Optical micrographs of the nLEDs dispersed on Si substrates. **b**, Ga 3d state ratios estimated using XPS. Fitting of XPS core-level spectra of dry-etched nanorods for Ga 3d (**c**) and N 1s (**d**). XPS core-level spectra for Si 2p (**e**), O 1s (**f**) and C 1s (**g**).

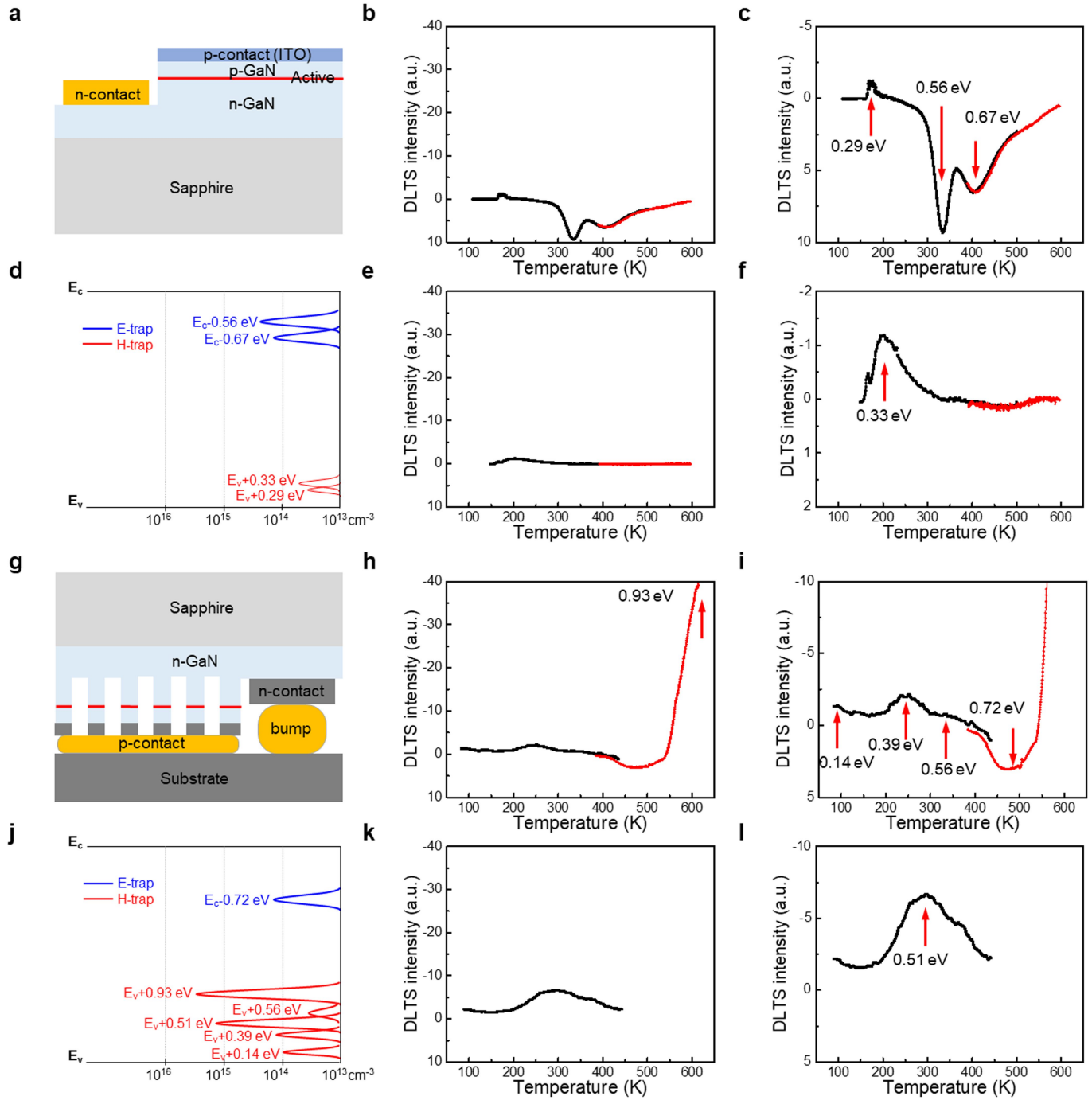

Extended Data Fig. 7 | Analysis of trap levels and their concentrations using DLTS. a–**f**, Bulk LED chip. **g**–**l**, nLED-array chip. **a**,**g**, Schematic of the chip. DLTS spectra obtained at forward bias (**b**,**h**) and enlarged spectra (**c**,**i**) in the region around the peak. DLTS spectra obtained at reverse bias (**e**,**k**) and enlarged spectra (**f**,**l**) in the region around the peak. **d**,**j**, Trap levels with their concentrations. They clearly show that the hole traps are dominant, with high concentrations in the nLED-array chip.

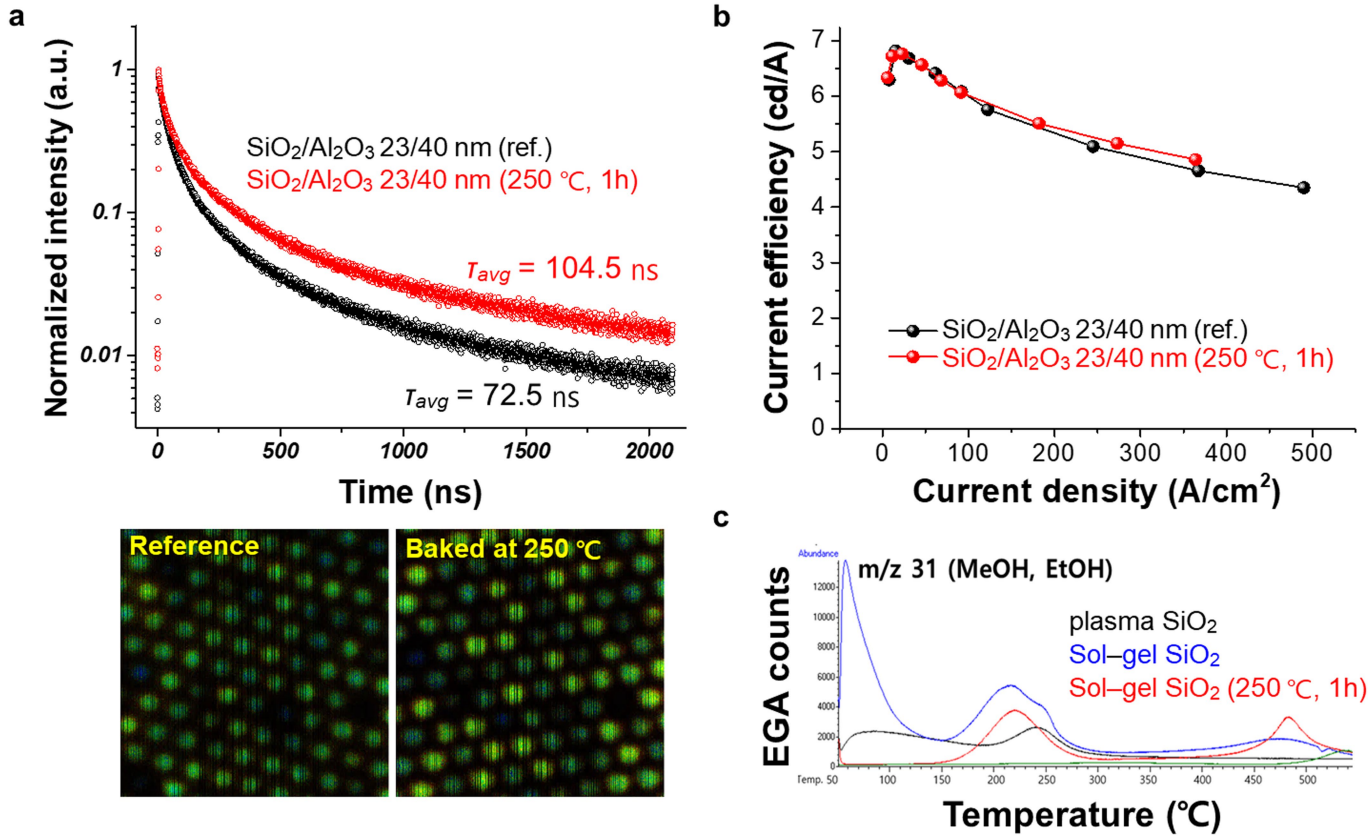

Extended Data Fig. 8 | Post-treatments of the sol–gel SiO_2-coated nLEDs. **a**, PL decay traces of the nLEDs averaged over the areas indicated in the images below. The carrier lifetime increased after baking the sample at 250 °C for 1 h. **b**, The EL efficiency versus current density of the nLEDs in a pixel structure. The EL performance is the same before and after the annealing. At a high current injection, the EL efficiency is slightly increased. **c**, Comparison of outgassing between the SiO_2 layers using pyrolysis–gas chromatography–mass spectrometry with evolved gas analysis–mass spectrometry.

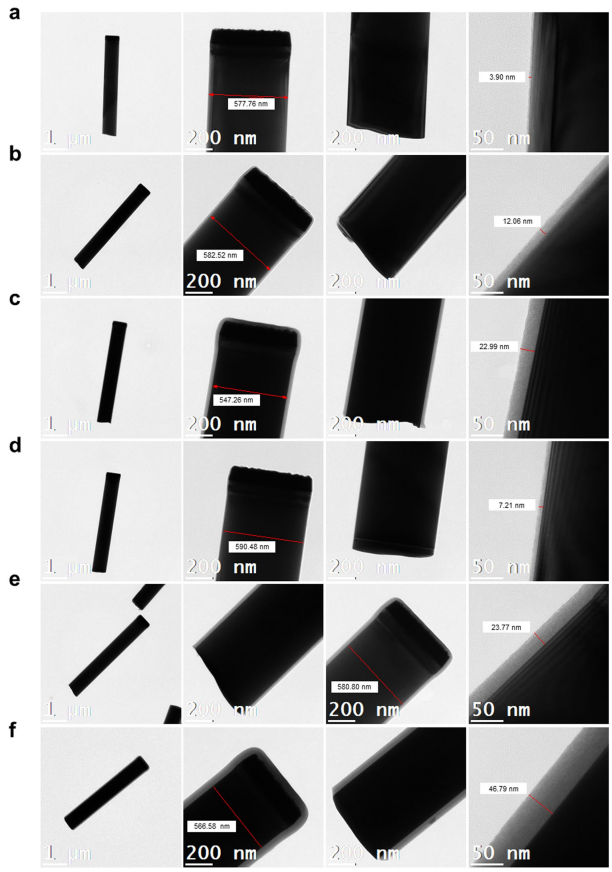

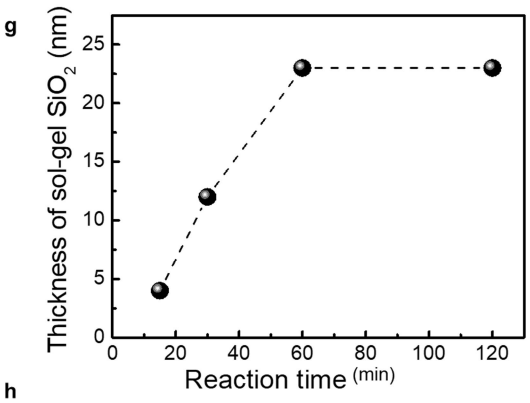

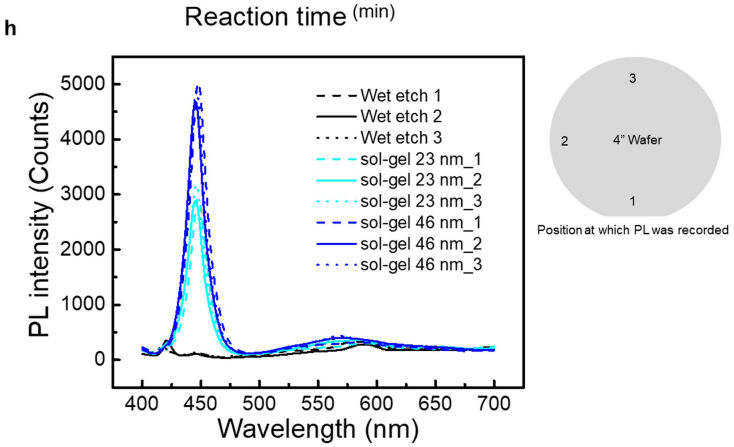

Extended Data Fig. 9 | Synthesis of SiO_2 passivation layer using the sol–gel method. a–**c**, Transmission electron microscopy images of nLEDs passivated with sol–gel SiO_2 at reaction times of 15 min (**a**), 30 min (**b**) and 60 min (**c**). **d**–**f**, In addition, the reaction was repeated twice under the same synthesizing conditions to increase their thicknesses. **g**, The thickness of the SiO_2 layer was saturated at 23 nm after reaction for 60 min. **h**, PL intensities of the nanorods. We obtained the PL spectra from three different positions on a 4-inch wafer. The variation in the PL intensity with respect to the position is small. Furthermore, the PL intensity increased with an increase in the thickness of the sol–gel SiO_2 layer.

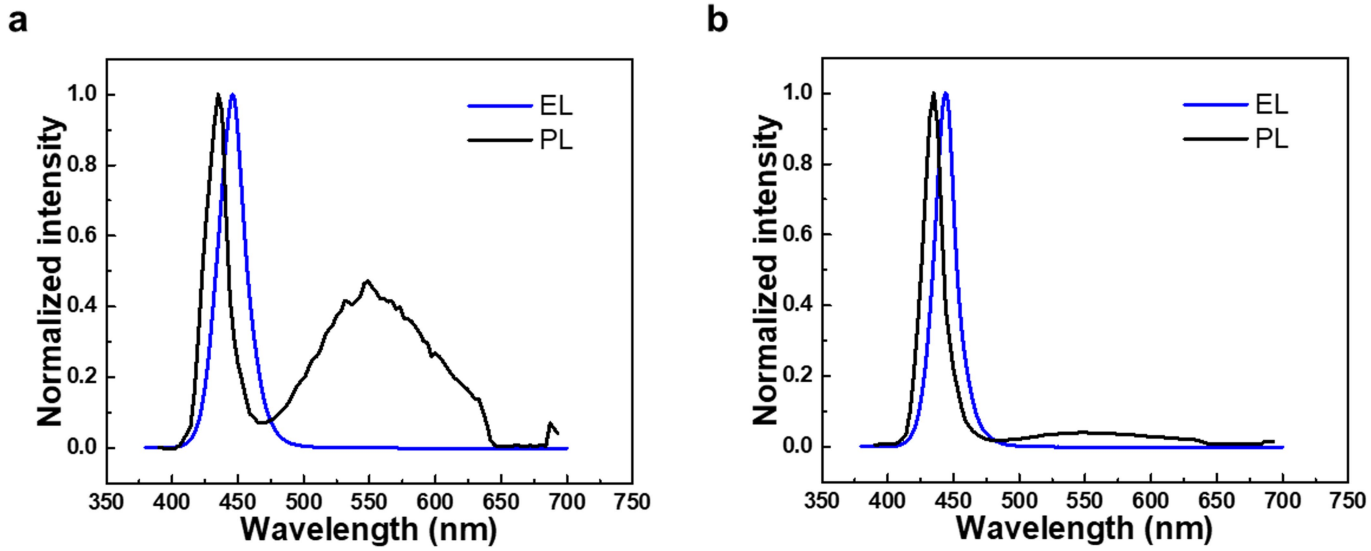

Extended Data Fig. 10 | Comparison between PL and EL spectra. a, Plasma-enhanced ALD SiO_2 passivation. **b**, Sol–gel SiO_2 passivation. The EL spectra are obtained at a current density of 10 mA cm^{-2}, which is near the peak EQE position.

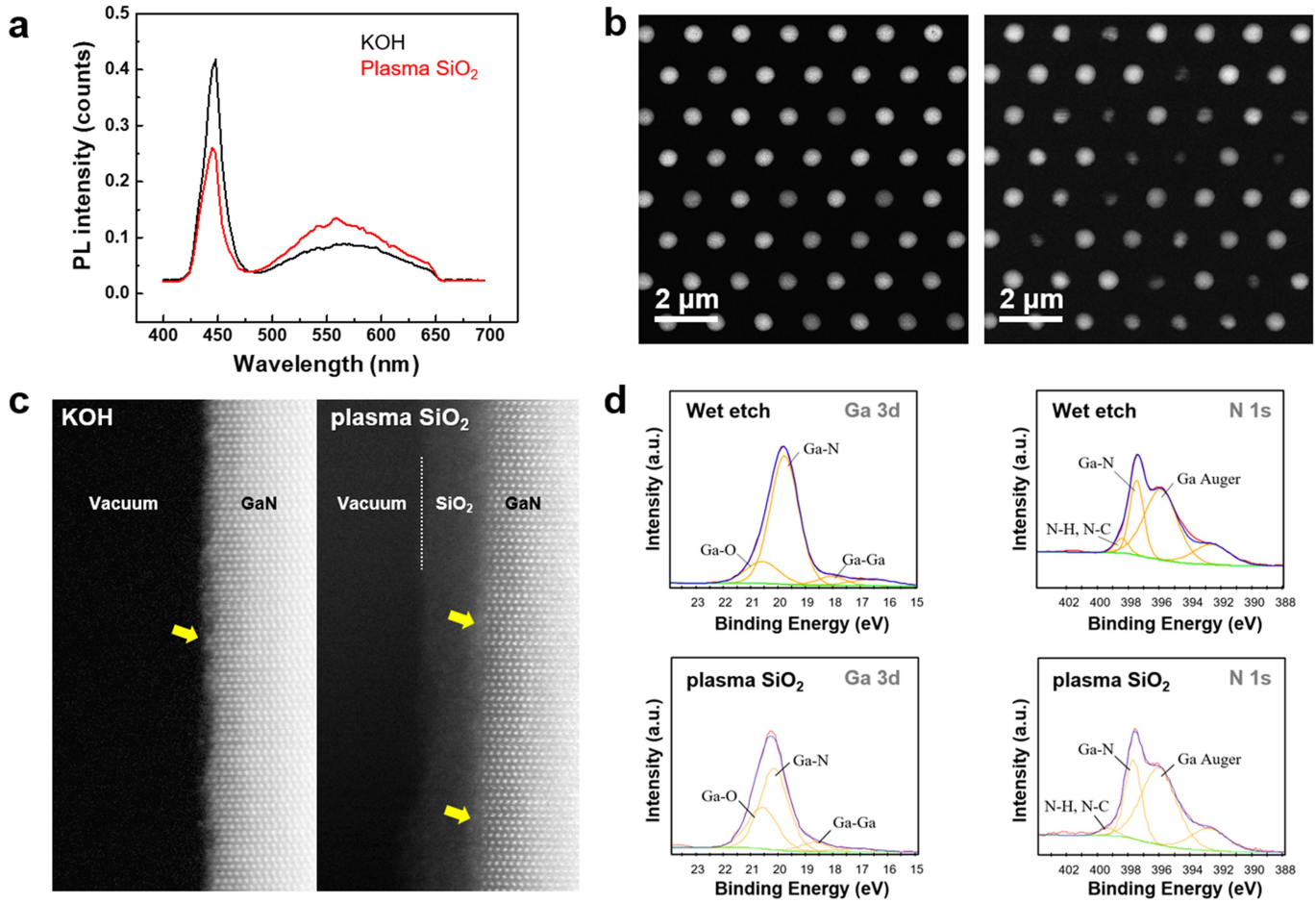

Extended Data Fig. 11 | Comparison between KOH wet etching and KOH wet etching plus plasma-enhanced ALD SiO_2 passivation process. a, **b**, PL spectra (**a**) and monochromatic CL images at 445 nm (**b**) of the nanorods for KOH wet etching and plasma ALD SiO_2 deposited. **c**, HAADF-STEM images of the nanorods' sidewalls. The yellow arrows indicate the native GaOx for the KOH case and the passivation-generated GaOx for the plasma SiO_2 case. **d**, XPS core-level spectra of the nanorods: Ga 3d and N 1s.

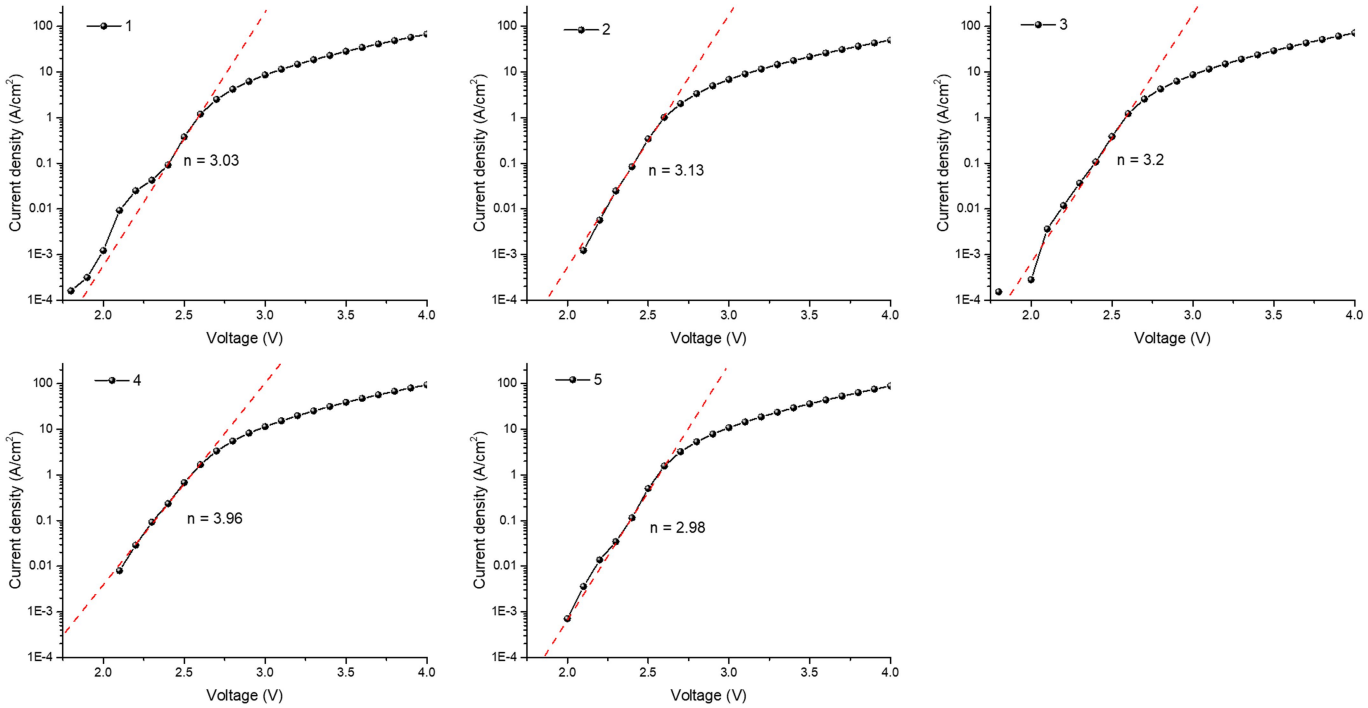

Extended Data Fig. 12 | Extraction of the ideality factor. The dashed red lines represent the linear fittings for calculating the ideality factor in the J–V curves of devices with the plasma-enhanced ALD SiO_2 passivation.